SPACE Conferences and Exposition
13 - 16 September 2016, Long Beach, California
AIAA/AAS Astrodynamics Specialist Conference

Stability of a Deployable Drag Device for Small Satellite Deorbit

Alexandra C. Long* and David A. Spencer†
Georgia Institute of Technology, Atlanta, GA, 30332-1510, USA

Orbital debris has crossed a threshold of critical density in Low Earth Orbit where the number of debris objects will grow exponentially due to collisions unless actively mitigated. Recent announcements of commercial small satellite constellations indicate interest in deploying hundreds to thousands of micro-satellites into Low-Earth Orbit at altitudes ranging from 1,000-1,200 km, in order to provide global internet service. These constellations create a great need for a standard system for deorbit to help mitigate the orbital debris problem. This paper describes a deployable drag device that leverages recent advancements in thin membrane deployable structures to create a passive aerodynamically stable drag sail that will ensure a satellite deorbits within 25 years regardless of its functionality. The aerodynamic stability of the drag device is evaluated for orbit altitudes ranging from 400 to 600 km, while varying the apex half-angle of the square pyramid drag sail from 65 to 85 deg. An apex half-angle of 80 or 85 deg provides passive stability for most conditions at orbit altitudes of 500 km and lower. It is shown that transparent CP1 is preferable to aluminized sail material for aerodynamic stability, due to the reduced solar torques.

Nomenclature

A	Area of sail, m^2
B	Non-Lambertian coefficient (see subscripts)
C	Coefficient (see subscripts)
h	Altitude, km
I	Moment of inertia about a body axis (see subscripts), kg-m^2
L	Boom length, m
M	Moments (see subscripts), N-m
n	Mean orbital motion
P_{rad}	Solar radiation pressure constant at Earth, 4.56x10^{-6} N/m^2
$\tilde{r}$	Fraction of photons to be reflected by sail
$\vec{R}_c$	Position vector of the center of mass of the sail system from the Earth's center, m
s	Speed ratio of the freestream,
T	Temperature, K (see subscripts)
V	Velocity, m/s (see subscripts)
α	Angle of attack, radians
β	Side slip angle, radians
γ_1	Angle between freestream and normal vector, radians
γ_2	Angle between Sun-sail system vector and normal vector, radians
ε	Fraction of photons reflected specularly
ϵ	Emissivity
μ	Gravitational constant for Earth, 398600.4 km^3/s^2
ϕ	Apex half-angle of sail, radians
ρ	Atmospheric density, kg/m^3

*Graduate Research Assistant, Daniel Guggenheim School of Aerospace Engineering, AIAA Student Member
†Professor of the Practice, Daniel Guggenheim School of Aerospace Engineering, AIAA Member

σ	Momentum accomodation coefficient (see subscripts)
θ_1	Roll angle, radians
Ω	Right ascension of the ascending node, degrees
ω	Components of angular velocity in the body frame, radians/sec
$\hat{\mathbf{e}}_\odot$	Unit vector from sail surface to the sun in flow frame

Subscript

b	Back of sail
D	Drag force
f	Front of sail
i	Variable number
L	Lift force
N	Normal force
P	Pressure
T	Tangential force
w	Wall condition
τ	Shear pressure
∞	Freestream condition
x, y, z	Relating to the corresponding body axis
$1, 2, 3$	Relating to the corresponding body axis

I. Introduction

Orbital debris is a growing problem in low-Earth orbit; it has crossed a threshold of critical density where the number of debris objects will grow exponentially due to collisions unless actively mitigated. Recently, there have been a number of announcements about commercial small satellite constellations indicating interest in deploying hundreds to thousands of micro-satellites into Low-Earth Orbit (LEO) at altitudes ranging from 1,000-1,200 km, in order to provide global internet service.[1,2,3] These constellations will put their satellites in orbits with the same altitude and inclination, but different right ascension of ascending node and argument of perigee. For example, OneWeb plans on having a constellation consisting of 18 orbital planes with an inclination of 87.9°, each with 40 satellites.[4] The need to deorbit these small satellites at the end of their operational lifetime is apparent. A 100 kg satellite with a 0.25 m^2 frontal area would take more than 100 years to deorbit naturally from an 1,100 km circular equatorial orbit. These constellations create a great need for a standard system for deorbit to help mitigate the orbital debris problem.

A deployable drag device (D^3) can leverage recent advancements in thin-membrane deployments for solar sails. There is significant current research into solar sail design and test, as well as recent test flights of small-scale solar sails. NanoSail-D, launched by NASA Marshall with a 10 m^2 drag area,[5,6] and Lightsail-A, launched by The Planetary Society with a 32 m^2 drag area, are examples of successfully deployed solar sails.[7,8] The D^3 system leverages these design concepts to provide a low-cost approach to accelerate the deorbit of micro-satellites.

A trade study was conducted to determine the baseline requirements for the D^3 system.[9] The study evaluated thin-membrane drag sails, inflatables, and tethers in comparison with a propulsive deorbit burn. From this trade study, thin-membrane drag devices were determined to be favored in terms of performance, reliability, and cost. The D^3 system is packaged in a 6U volume, from an enclosure that is attached to the satellite using a standard bolt-on interface. It will be completely passive once deployed, and be capable of deorbiting small satellites from orbit altitudes of 1,000-1,200 km within 25 years. A design requirement of the drag device is that it will passively trim to a maximum drag attitude perpendicular to the flow direction. This stability, combined with a deployment timer, allows this deorbit system be independent of the status of the satellite itself. It will be deployed after a preprogrammed time, and the system will include a standard interface to update the default deployment date if desired. This ensures that the satellite will be deorbited even if there is a mission ending event, without the need for an active debris removal system.

II. Stability Analysis

The sail system for this analysis consists of a 6U enclosure connected to a square pyramid with no bottom face. There are a few key parameters that define the shape and size of the sail that will be discussed, as well as the angles that are used to define the orientation of the sail throughout the analysis. The first step of the analysis was the initial sizing of the sail to ensure that it will deorbit the satellite within 25 years to comply with international standards. The next step is to analyze the attitude of the sail as it changes due to the main disturbing torques encountered by a satellite in LEO. These torques are aerodynamics, gravity gradient, and solar radiation pressure. These will be described in this section, along with a description of the simulation used to evaluate performance.

II.A. Sail Description

The D^3 sail is split into four triangular quadrants that are made from a thin membrane only a few microns thick, like Mylar or CP1. These quadrants are supported by four strain deployed booms that make up the edges of the pyramid. The key components of the sail are shown in Fig 1. The sail is defined by two important design variables: boom length, L, and the apex half-angle, ϕ. The apex half-angle is defined as the angle between one boom and the center axis, so for larger values of ϕ, the flatter the sail. That also means that if the boom length is kept constant, the base area of the pyramid decreases as ϕ decreases. It can be seen that this system is easily modeled by a series of flat plates for the different analyses.

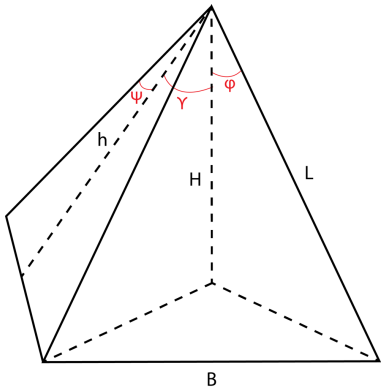

Figure 1: Diagram of the square pyramid sail with variable definitions.

The coordinate system was chosen to follow conventional flight dynamics body axes with the x direction along the longitudinal axis of the vehicle, and the y and z directions forming a right-handed set perpendicular to the x-axis.[10] The coordinate systems can be seen in Fig. 2a. The flow frame has f_1 in the direction of movement, f_3 pointing in the nadir direction, and f_2 completing the right hand set. The rotation of the solar sail is defined by angle of attack, α, and side slip angle, β. They can be seen in Figs. 2b and 2c. Note that β is defined as positive for a negative rotation about the z-axis. For stability, restoring moments are required to ensure the sail will come back to the maximum drag attitude if perturbed. This means a negative restoring moment about the y-axis (pitch) for positive perturbations in α, and a positive restoring moment about the z-axis (yaw) for perturbations in β.

II.B. Deorbit Analysis

The first step of this analysis was to determine an initial size of the sail that will deorbit the satellite within 25 years to comply with international standards. This was conducted using the General Mission Analysis Tool (GMAT), an open source mission analysis tool developed by NASA Goddard Space Flight Center.[11] This tool lets you set the orbit parameters, and it will propagate the orbit until a desired end condition is reached. For this analysis, the start date was set to July 1, 2020 at 12:00 pm, with a circular orbit inclined at 87.9°, to match the OneWeb concept. The right ascension of ascending node, argument of perigee, and true anomaly were all set to 0°. The gravity model was set to JGM-2 of degree 4 and order 4. The atmosphere model was MSISE90. Solar radiation pressure was not included. The stopping condition was set to an altitude of 110 km. The simulation was run for initial altitudes of 1,100 km and 1,200 km, satellites masses

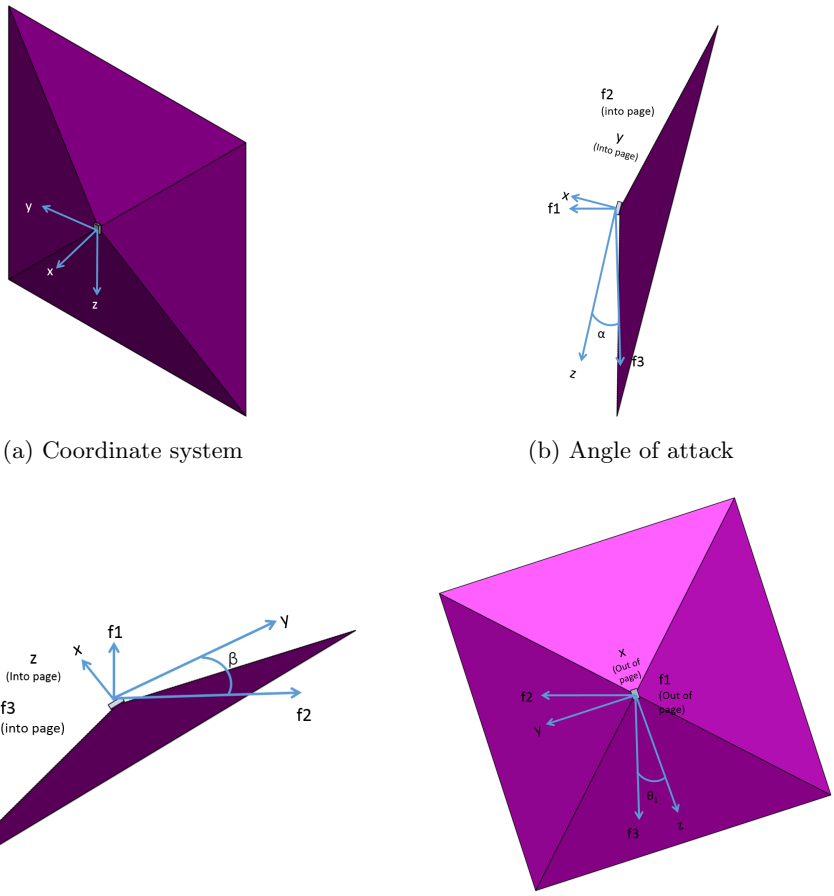

(a) Coordinate system

(b) Angle of attack

(c) Side slip angle

(d) Roll angle

Figure 2: Definition of coordinate system and orientation angles used in the drag sail analysis

of 100 and 150 kg, and a number of different drag areas. The results can be seen in Figs. 3 and 4. They demonstrates that drag sail area is very dependent on both the mass of the satellite and the initial altitude of the orbit. The required area does not scale linearly with increasing altitude and mass. It can be seen that in order to deorbit a 150 kg satellite from 1,200 km, a drag area of 195 m^2 is required. The 125 m^2 drag area can deorbit a 100 kg satellite from 1,200 km or a 150 kg satellite from 1,100 km. Two different versions of the D^3 device will be available depending on application.

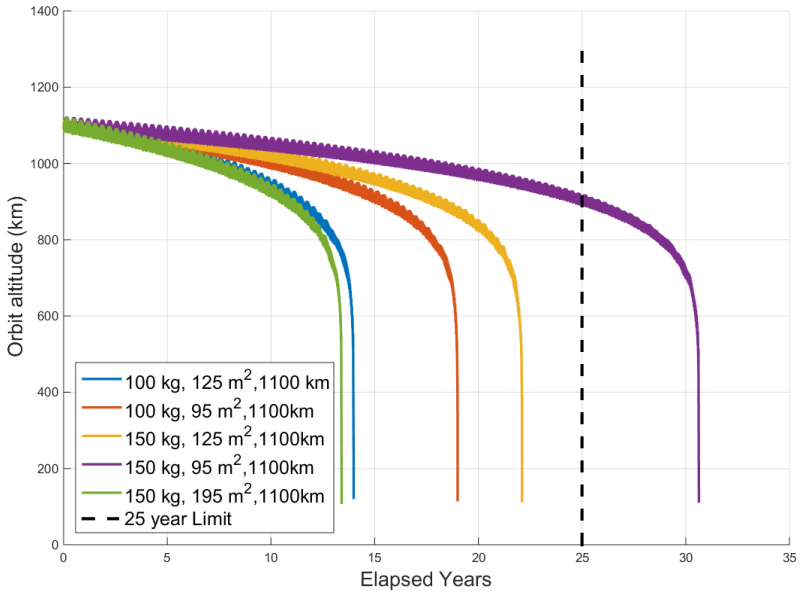

Figure 3: GMAT simulation results starting at an altitude of 1,100 km with different satellite masses, and drag area.

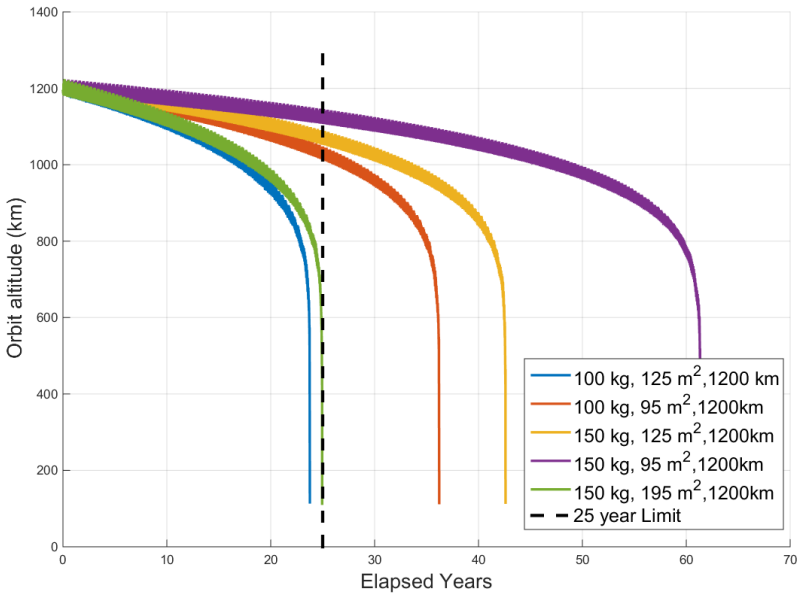

Figure 4: GMAT simulation results starting at an altitude of 1,200 km with different satellite masses, and drag area.

II.C. Torque Definitions

The aerodynamic forces and moments were calculated using the analytically derived equations proposed by Hart et al.[12] These equations are derived by integrating the coefficients of pressure and shear pressure shown in Eqs. (1) and (2) over the surface of each plate, where V_∞ is the freestream velocity of the air, T_∞ is the freestream static temperature of the air in Kelvin, T_w is the temperature of the surface, and σ_N and σ_T are the momentum accommodation coefficients in the normal and tangential directions. Eq. (4) defines the

angle γ_1 as the angle between the freestream and the vector parallel to the surface. The function $erf(x)$ is the error function which is found when integrating the normal distribution.[13]

$$C_p = \frac{1}{s^2}\left[\left(\frac{2-\sigma_N}{\sqrt{\pi}} s\sin(\gamma_1) + \frac{\sigma_N}{2}\sqrt{\frac{T_w}{T_\infty}}\right) e^{-(s\sin\gamma_1)^2} + \left\{(2-\sigma_N)\left((s\sin\gamma_1)^2 + \frac{1}{2}\right) + \frac{\sigma_N}{2}\sqrt{\frac{\pi T_w}{T_\infty}} s\sin\gamma_1\right\}(1+\mathrm{erf}(s\sin\gamma_1))\right] \tag{1}$$

$$C_\tau = -\frac{\sigma_T\cos\gamma_1}{s\sqrt{\pi}}\left[e^{-(s\sin\gamma_1)^2} + \sqrt{\pi} s\sin\gamma_1\,(1+\mathrm{erf}(s\sin\gamma_1))\right] \tag{2}$$

$$s = \frac{V_\infty}{\sqrt{2RT_\infty}} \tag{3}$$

$$\sin\gamma_1 = -\hat{\mathbf{V}}_\infty \cdot \hat{\mathbf{n}} \tag{4}$$

The gravity gradient torque for the system was calculated using Eq. (5), where $\vec{R_c}$ is the position vector of the center of mass of the sail system from the Earth's center, and $\hat{I}$ is the inertia dyadic of the sail-satellite system.[14]

$$\vec{M} = \frac{3\mu}{R_c^5}\vec{R_c}\times\hat{I}\cdot\vec{R_c} \tag{5}$$

The solar radiation pressure torque was calculated in a similar procedure as the aerodynamic torques but substituting the normalized vector between the sail and the sun for the normalized velocity vector and substituting Eqs. (6) and (7)[15] for Eqs. (1) and (2). $P_{rad} = 4.563\times10^{-6} N/m^2$ is the nominal solar radiation pressure constant at 1 AU from the sun,[14] $\tilde{r}$ is the fraction of photons to be reflected by the sail, ε is the fraction of photons to be reflected specularly, ϵ is the emissivity of the front and back of the sail depending on the subscript, and B is the non-Lambertian coefficient of the front and back of the sail. Eq. (8) defines the angle between the normal vector of the sail and the unit vector from the Sun to the sail. Notice that this is defined opposite of γ_1 used in the aerodynamic formulas.

$$C_n = P_{rad}\left[(1+\tilde{r}\varepsilon)\cos^2\gamma_2 + B_f(1-\varepsilon)\tilde{r}\cos\gamma_2 + (1-\tilde{r})\frac{\epsilon_f B_f - \epsilon_b B_b}{\epsilon_f+\epsilon_b}\cos\gamma_2\right] \tag{6}$$

$$C_t = P_{rad}\,(1-\tilde{r}\varepsilon)\cos\gamma_2\sin\gamma_2 \tag{7}$$

$$\cos\gamma_2 = -\hat{\mathbf{e}}_\odot \cdot \hat{\mathbf{n}} \tag{8}$$

II.D. Stability Simulation Description

The stability analysis investigates the contributions of the different torques for varying apex half-angles of the square pyramid drag sail, and for a range of orbit altitudes. As described in Wie,[14] the non-linear equations of motion for an orbiting rigid body about body-fixed principal axes are integrated over time. This is accomplished by integrating the non-linear equations of motion of an orbiting rigid body about body-fixed principal axes described by Wie. Equation 9 shows the kinematic differential equations, where the orientation angles are from Fig 2 with $\theta_2 = \alpha$ and $\theta_3 = -\beta$. Equations 10 are the dynamic equations of motion with all of the disturbance torques described earlier.[14]

$$\begin{bmatrix}\dot{\theta}_1\\ \dot{\theta}_2\\ \dot{\theta}_3\end{bmatrix} = \frac{1}{\cos\theta_1}\begin{bmatrix}\cos\theta_2 & \sin\theta_1\sin\theta_2 & \cos\theta_1\sin\theta_2\\ 0 & \cos\theta_1\cos\theta_2 & -\sin\theta_1\cos\theta_2\\ 0 & \sin\theta_1 & \cos\theta_1\end{bmatrix}\begin{bmatrix}\omega_1\\ \omega_2\\ \omega_3\end{bmatrix} + \frac{n}{\cos\theta_2}\begin{bmatrix}\sin\theta_3\\ \cos\theta_2\cos\theta_3\\ \sin\theta_2\sin\theta_3\end{bmatrix} \tag{9}$$

$$
\begin{aligned}
I_x\dot{\omega}_1 &= (I_y - I_z)\omega_2\omega_3 - 3n^2(I_y - I_z)\sin\theta_1\cos\theta_1\cos^2\theta_2 + M_{x,aero} + M_{x,SRP} \\
I_y\dot{\omega}_2 &= (I_z - I_x)\omega_1\omega_3 + 3n^2(I_z - I_x)\cos\theta_1\cos\theta_2\sin\theta_2 + M_{y,aero} + M_{y,SRP} \\
I_z\dot{\omega}_3 &= (I_x - I_y)\omega_1\omega_2 + 3n^2(I_x - I_y)\sin\theta_1\sin\theta_2\cos\theta_2 + M_{z,aero} + M_{z,SRP}
\end{aligned} \tag{10}
$$

The inputs to the simulation were orbital elements, the start date and time, and the physical properties of the sail-satellite system. As with the deorbit analysis, the system was in a circular orbit inclined at 87.9°, starting on July 1, 2020 at 12:00 pm. The mass of the satellite portion was set to 150 kg. The sail size was determined by the length of the booms and the apex half-angle. The boom length was set to 8 m because that achieves an 125 m^2 drag area for an apex half-angle of 80°. The apex half-angle and the altitude were varied to determine how the aerodynamic stability varies. Table 1 lists the values of each parameter that was investigated. The sail was considered stable if the values of α and β stayed between $\pm 90°$ for the length of the simulation.

The stability due to SRP is much more complicated because it depends on the direction of the sun-sail unit vector. Fixing the start date meant that the Sun was fixed in the sky relative to the Earth, but the vector relative to the sail changes as the sail moves throughout its orbit and as the right ascension of the ascending node of the orbit changes (Ω). For perspective, when $\Omega = 100°$, the orbit plane is nearly aligned with the sun vector as seen in Fig 5. Ω was used as an input of the simulation and varied to determine trends. To take into account the change in true anomaly, the position and velocity of the satellite were integrated at the same time as the attitude. The stability simulation was propagated over five full orbits. A switching function was used to turn off the SRP moment when the sail moved behind the Earth.

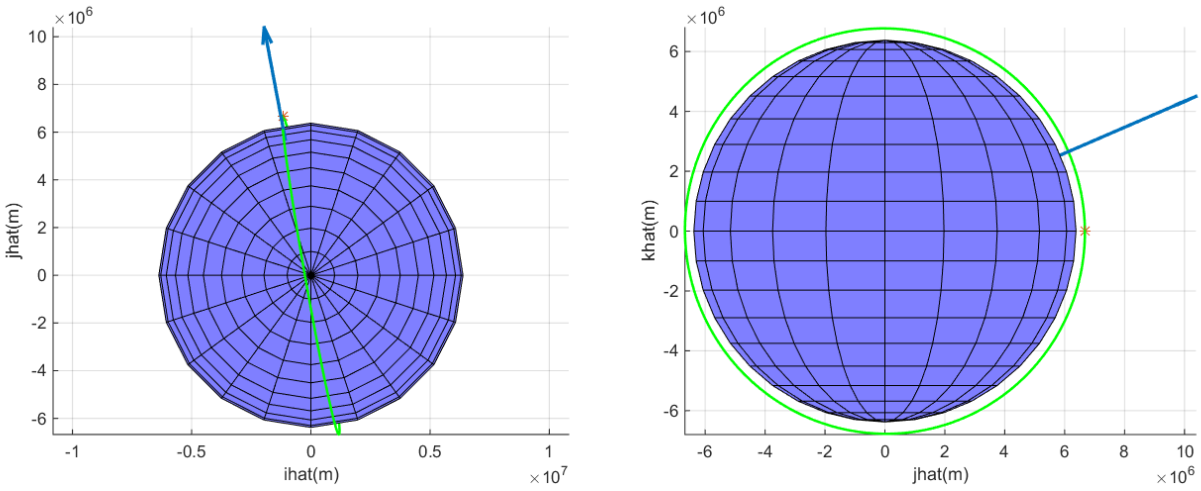

(a) (b)

Figure 5: The sun position on July 1, 2020 at noon, and the orbit with $\Omega = 100°$

Table 1: The values of the parameters run for the simulations.

ϕ (°)	65, 70, 75, 80, 85, 90
h (km)	350, 400, 450, 500, 525, 550, 580, 600
Ω (°)	0, 10, 90, 100, 180, 270

III. Stability Results

Cases were run for varying altitudes, apex half-angles, and orbital parameters. The results are separated into two parts. The first part discusses the effects of the parameters on each torque. The second part shows the results of the simulations, and sail stability is assessed. The final section describes the resulting baseline design for the drag device.

III.A. Gravity Gradient Torque

The first of the three disturbance torques is the gravity gradient torque. From Eq (5), it can be seen that this torque depends on the moments of inertia about a set of principal axes. The value of this torque about each axis depends on the orientation angles and the difference between the moments of inertia in the other two directions. For example, the gravity gradient torque about the x-axis is not very large because the difference between I_y and I_z is not very large. As the apex half-angle increases toward a flat sail, the gravity gradient torque in the y and z directions increase because the I_x goes toward the sum of the other two moments of inertia. This also depends on the value of n, the constant orbital rate, which is proportional to the inverse of the magnitude of the radius cubed. This means that the value of the torque decreases with increasing altitude, but it is a much smaller effect than the effect of altitude on the aerodynamic torque. The gravity gradient torque is smaller than the other two torques at altitudes less than 750 km.

III.B. Aerodynamic Torque

The aerodynamic torque is the second torque. The lower the altitude, the larger the drag force and aerodynamic moments because the atmosphere has a higher density. It can be seen in Fig. 6 that the aerodynamic drag of the sail decreases as the apex half-angle decreases. As the apex half-angle decreases, the magnitude of the restoring pitching moment due to the aerodynamic torque increases.

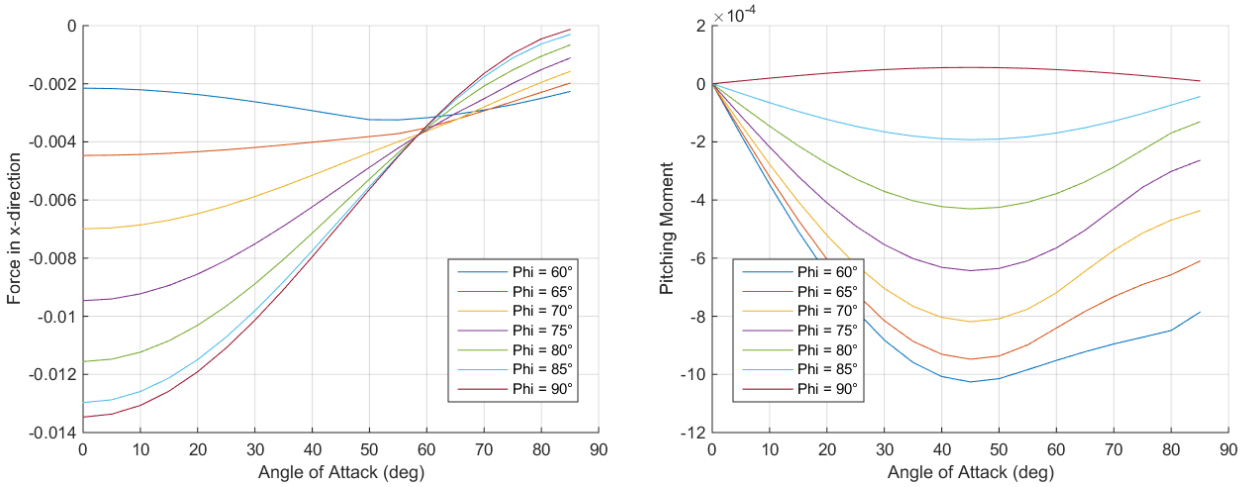

(a) (b)

Figure 6: The aerodynamic forces and moments at an altitude of 500 km due to different apex half-angles.

III.C. Torque due to Solar Radiation Pressure

The solar radiation pressure, on the other hand can create moments the help to restore the nominal attitude, but it can also create moments that disturb the sail, and sometimes both within the same orbit. This can be seen in Fig. 7. It shows the largest magnitude of each force for a range of angles of attack from 0°to 90°, throughout the entire orbit. Changing the Ω changes the magnitude and direction of the SRP, and it is large enough to compete with the aerodynamic torques. This disrupts the stability of the sail.

Most thin membrane structures have been solar sails, which require highly reflective membrane materials because they want to utilize the SRP for propulsion. This means adding an aluminum coating to naturally transparent materials like mylar, kapton, or CP1. In this case, SRP only hurts the function of the drag sail, so it would be better to not have that aluminum coating on the membrane. The next section shows how the attitude of the sail behaves over five orbits with and without the aluminum coating on the sail. The parameters for Eqs. (6) and (7) for the aluminized sail are shown in Table 2.

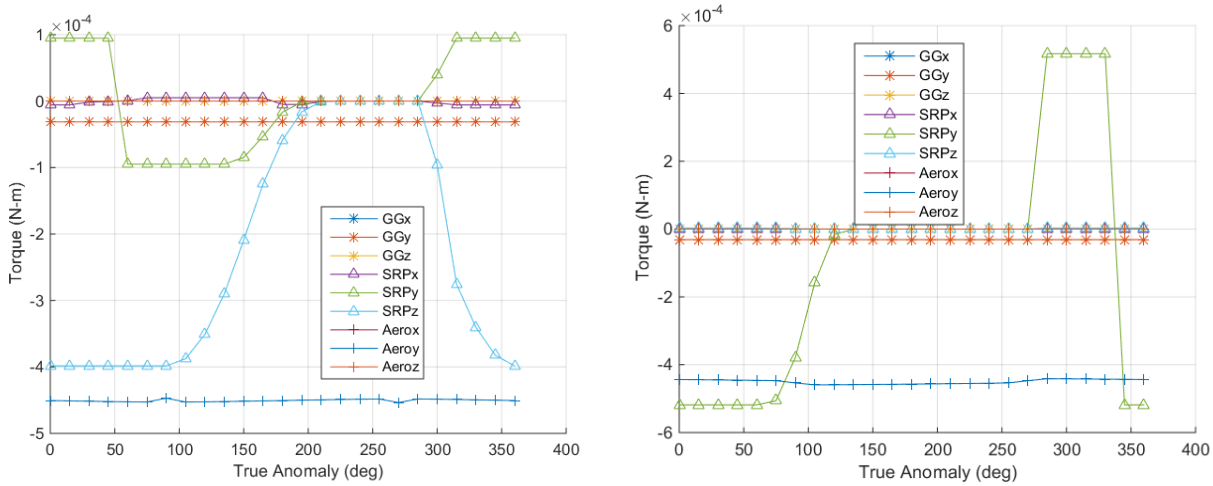

(a) $\Omega = 10°$ (b) $\Omega = 100°$

Figure 7: The maximum magnitude of each torque over a range of angles of attack throughout the entire orbit at an altitude of 500 km and an apex half-angle of 80°, and aluminized mylar as the sail material.

Table 2: Parameters for an aluminized sail.[15,16]

$\tilde{r}$	ε	ϵ_f	ϵ_b	B_f	B_b
0.88	0.92	0.05	0.55	0.79	0.55

III.D. Attitude Simulation Results

The simulations showed that the aerodynamic and gravity gradient torques mostly oscillate around the nominal attitude with a steady amplitude, with the aerodynamic torques having a higher frequency than the gravity gradient. The SRP is highly dependent on the orbit, and tends to increase the orientation angles so that the attitude is no longer in a stable regime. When using aluminized sail materials, there were only a few cases that were stable over the 5 orbit period, all of which were at altitudes at 400 km or below. The most common stable cases were when $\phi = 80°$and 85°, with a couple cases where ϕ is smaller. The flat plate case always tumbled. All of the stable cases with an aluminized sail material is shown in Table 3 and Fig 8.

Table 3: The cases where the sail-satellite system was stable over 5 orbits with an aluminized membrane sail.

ϕ (°)	h (km)	Ω (°)
85	400	10, 100, 270
80	400	10
80	350	10, 180
70	400	100
65	400	10, 180

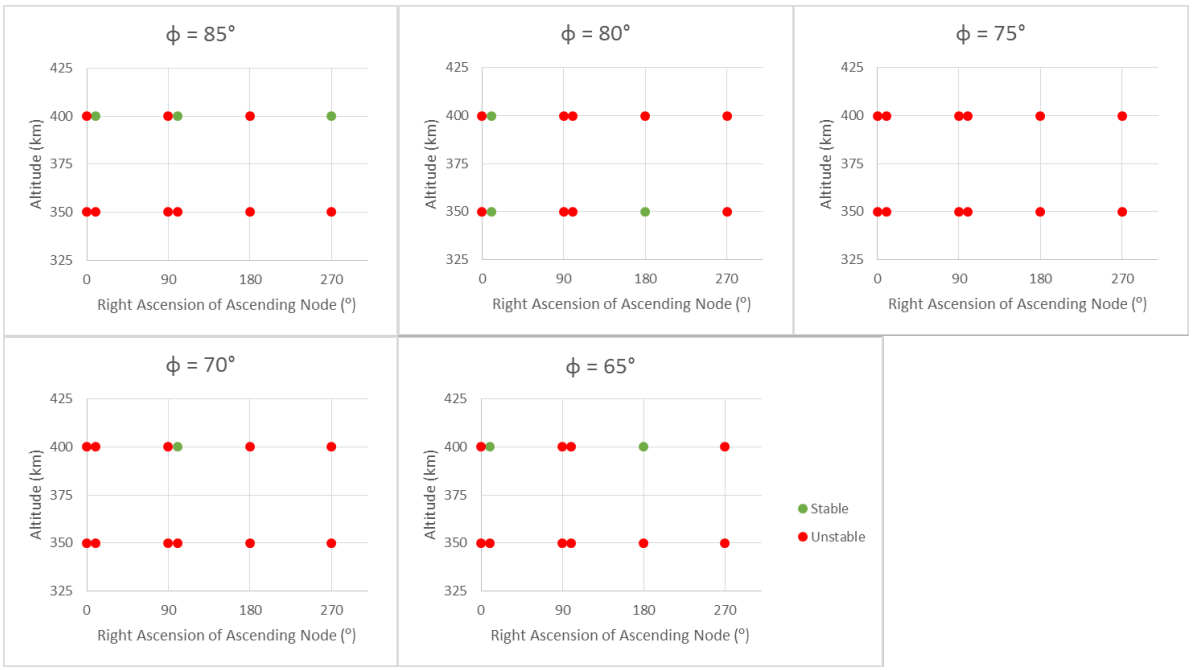

Figure 8: Graphical representation of the simulation results with an aluminized CP-1 sail. Higher altitudes with no stable cases were not included.

Figure 9 shows a stable case, and Fig. 10 shows an unstable case. The angular velocity components for the first case stayed small in magnitude, while the angular velocity components grew much larger at about the same time that the angles grew. In Fig. 9b, the pitching rate (ω_2) does not oscillate about 0 rad/sec, instead it oscillates about 1.1×10^{-3} rad/sec, which is the mean orbital motion. This is consistent with the system aligning the x-axis with the flow direction throughout the orbit.

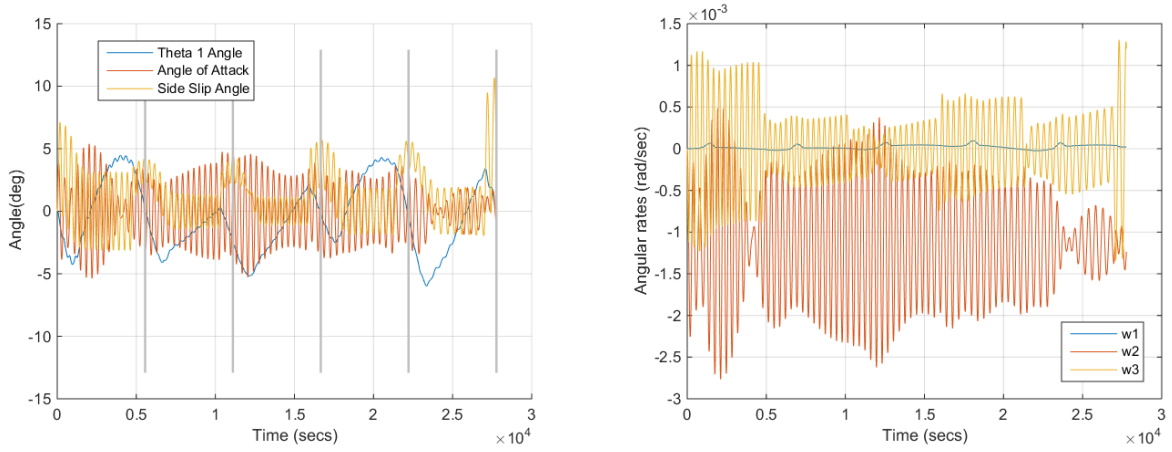

(a) Angle history over 5 orbits

(b) Body fixed angular velocities over 5 orbits

Figure 9: The simulation results for a stable configuration with aluminized sail material. $\phi = 80°$, $h = 400$ km, $\Omega = 10°$.

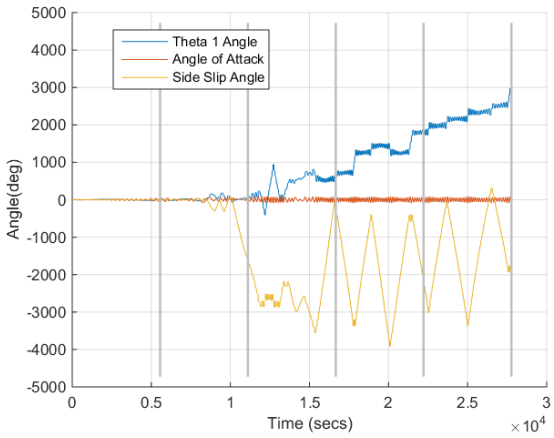

(a) Angle history over 5 orbits

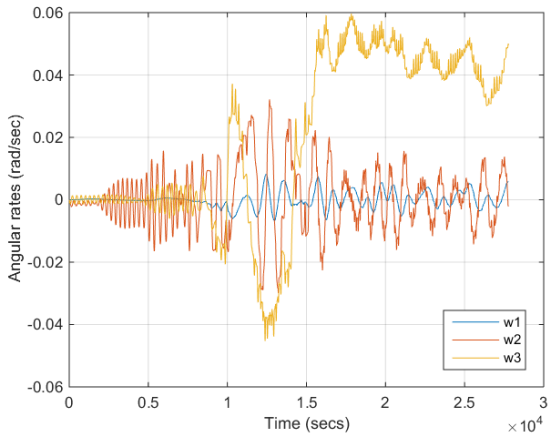

(b) Body fixed angular velocities over 5 orbits

Figure 10: The simulation results for an unstable configuration with aluminized sail material. $\phi = 70°$, $h = 400$ km, $\Omega = 10°$.

The instability can be predicted by looking at Fig. 11 with the derivatives of the rolling (L), pitching (M), and yawing (N) moments in terms of the angle of attack (α), side slip angle(β) and roll angle (θ_1), respectively, throughout the simulation. When these derivatives are negative, the angles are stable. Figure 11a shows that the pitching moment in terms of angle of attack and the yawing moment in terms of side slip angle are always negative, confirming the stability shown in Fig. 9. Figure 11b, on the other hand, has those derivatives negative until right before the point where the side slip angle grew to be larger than 90°, shown with a grey line. After that point, both the pitching moment and yawing moment are unpredictable, oscillating about zero. This is caused by the SRP. Figure 12 shows the moments created by each disturbance torque about each axis for the unstable case. Since instability starts with the side slip angle growing, Fig. 12d zooms in on the z-axis graph before the moment of instability. It can be seen at about 4800 seconds, the system comes out of eclipse and the SRP grows, increasing the side slip angle, which in turn increases the aerodynamic moments to a point where the system is no longer stable. That is the onset of instability. It can be seen that the moments in the other axes also become more chaotic starting at about 4800 seconds.

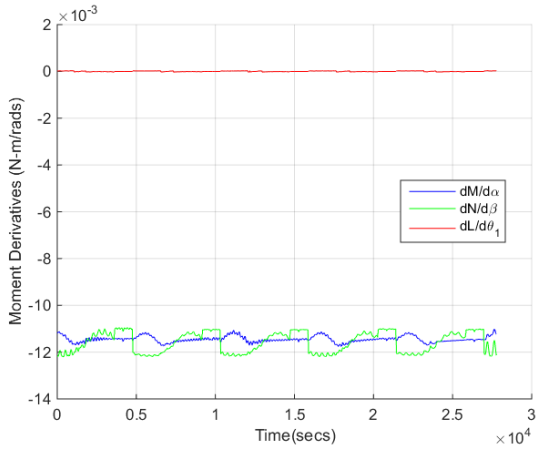

(a) Stable Case, $\phi = 80°$

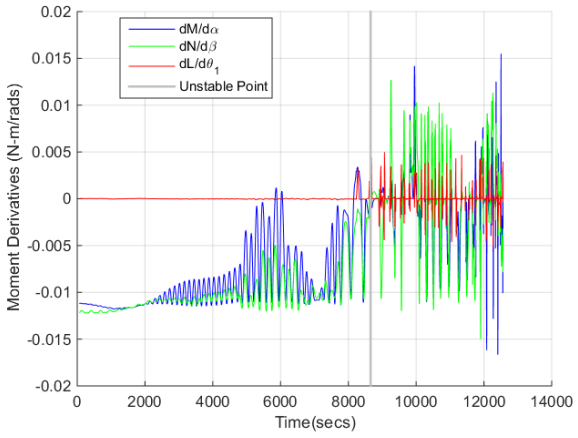

(b) Unstable Case, $\phi = 70°$

Figure 11: The moment derivatives due to each orientation angle throughout part of the simulation for the stable and unstable case.

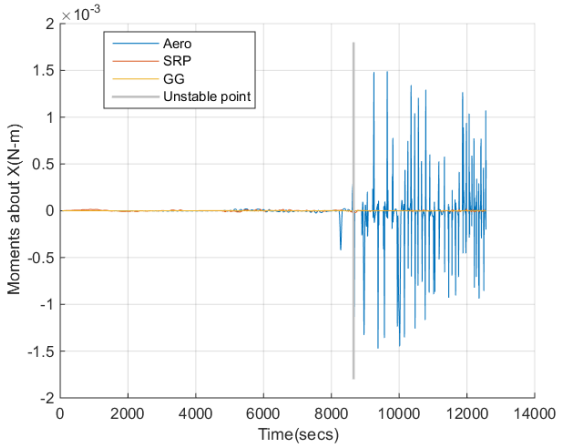

(a) Moments about x-axis

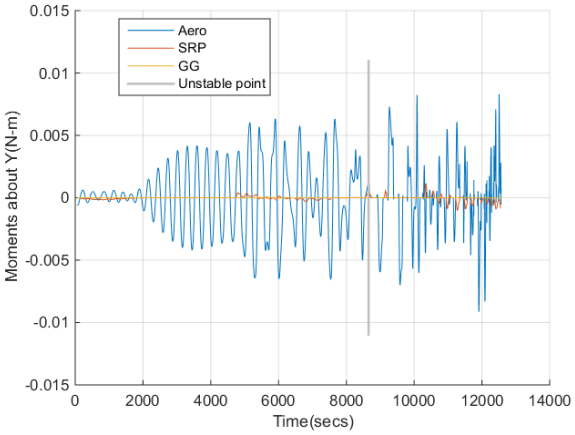

(b) Moments about y-axis

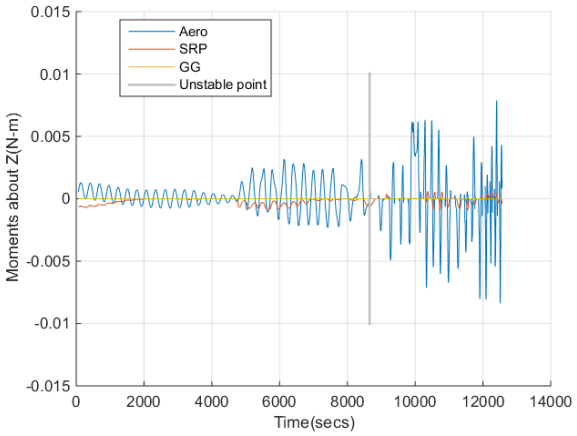

(c) Moments about z-axis

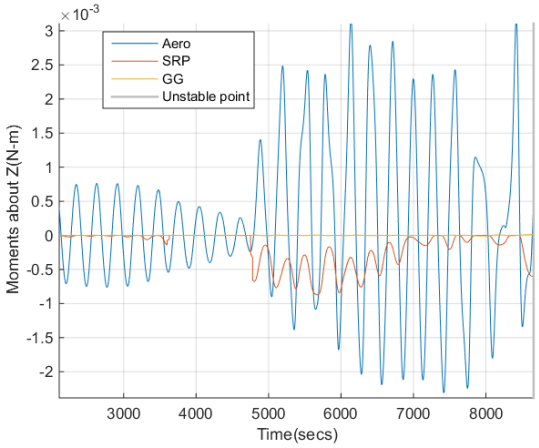

(d) Moments about z-axis zoomed in before instability

Figure 12: Moments about each axis due to the three torques for the beginning of the simulation for the unstable case with aluminized sail material. $\phi = 70°$, $h = 400$ km, $\Omega = 10°$.

The moment graphs for the stable case can be seen in Fig. 13. It can be seen that during eclipse, when the SRP is zero, the aerodynamic moments about the z-axis oscillate about zero, and when the system comes out of eclipse the SRP changes the side slip angle, but only enough so that the net moment stays the same. The SRP does not cause a large enough increase in side slip angle to push the system into the unstable regime. The SRP creates larger torques with the smaller apex half-angle because the sail will create a smaller angle with the vector toward the sun, as seen in Fig. 14. This angle is γ_2 from Eq. (6), and since the magnitude of the normal component is dependent on $\cos\gamma_2$, the smaller the value of γ_2 the larger the normal component of the SRP torque.

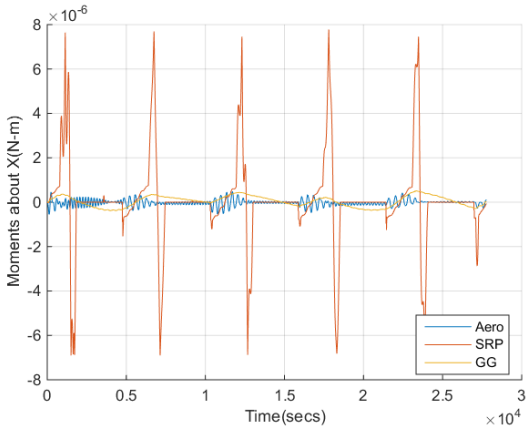

(a) Moments about x-axis

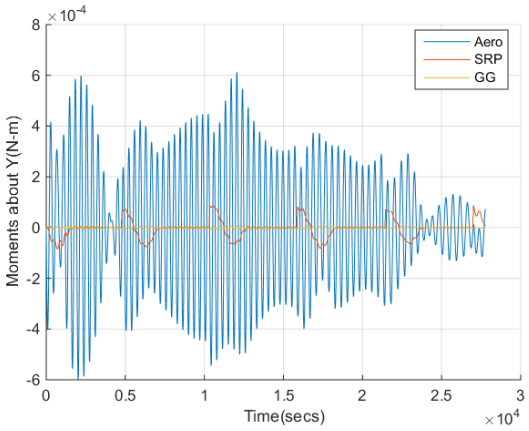

(b) Moments about y-axis

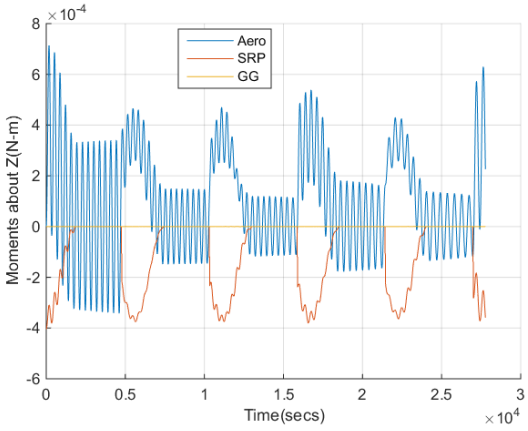

(c) Moments about z-axis

Figure 13: Moments about each axis due to the three torques for the beginning of the simulation for the stable case with aluminized sail material. $\phi = 80°$, $h = 400$ km, $\Omega = 10°$.

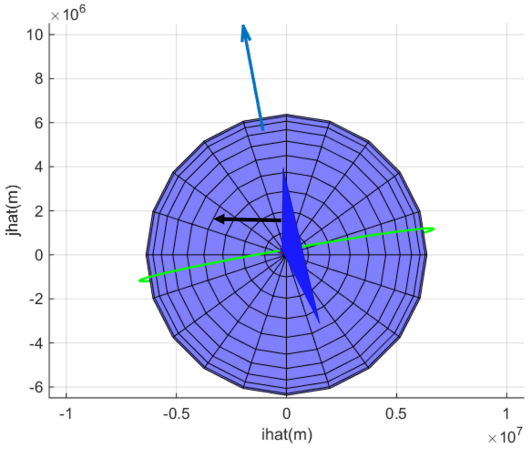

(a) $\phi = 80°$ sail in orbit about Earth

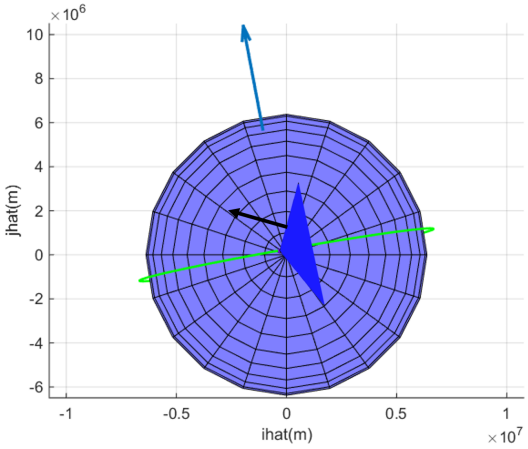

(b) $\phi = 70°$ sail in orbit about Earth

Figure 14: An exaggerated picture of the sails in orbit about the Earth with the sail normals and unit vector to the sun marked. The angle between these two vectors determines the SRP torque. $\Omega = 10°$.

It is not very useful for the design of a drag sail to show that only certain orbits enable the sail to be stable. As mentioned earlier, the next step was to investigate the stability when using a clear sail material instead of aluminized material. This changes the values used in Eqs. (6) and (7) to those shown in Table 4[a]. This means that the last term in Eq. (6) goes to zero because the properties of the front and back are the same.

Table 4: Parameters for a clear CP1 sail.

$\tilde{r}$	ε	ϵ_f	ϵ_b	B_f	B_b
0.88	0.09	0.55	0.55	0.55	0.55

Changing these parameters had the desired effect of reducing the SRP and increasing the cases of when the sail is stable. The stable cases are shown in Table 5 and Fig. 15. These simulations were not run for an altitude of 350 km because so many were stable at 400 km. An example is shown in Fig. 16. Many of the cases at altitudes of 500 and 525 km were stable for 4 orbits, and barely became unstable during the simulation.

Table 5: The cases where the sail-satellite system was stable over 5 orbits with a clear CP1 sail.

ϕ (°)	h (km)	Ω (°)
85	525	180
85	500	90, 100, 180, 270
85	450	0, 10, 90, 100, 180, 270
85	400	0, 10, 90, 100, 180, 270
80	450	0, 10, 90, 100, 180, 270
80	400	0, 10, 90, 100, 180, 270
75	525	270
75	500	100, 270
75	450	0, 10, 90, 100, 180, 270
75	400	0, 10, 90, 100, 180, 270
70	525	0, 100
70	500	90, 100, 180, 270
70	450	0, 90, 100, 270
70	400	10, 90, 100, 270
65	500	90, 100
65	450	90, 100, 270
65	400	90, 100, 270

[a]These values came from testing data provided by Andrew Heaton at NASA Marshall Spaceflight Center.

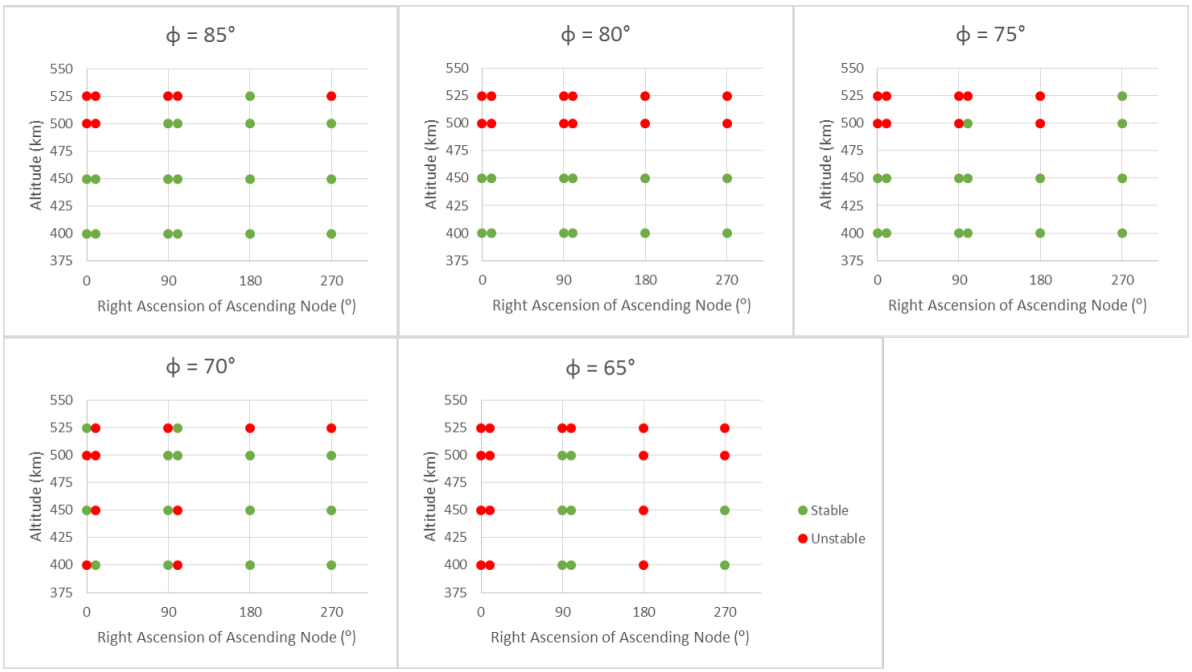

Figure 15: Graphical representation of the simulation results with a clear CP-1 sail. Higher altitudes with no stable cases were not included.

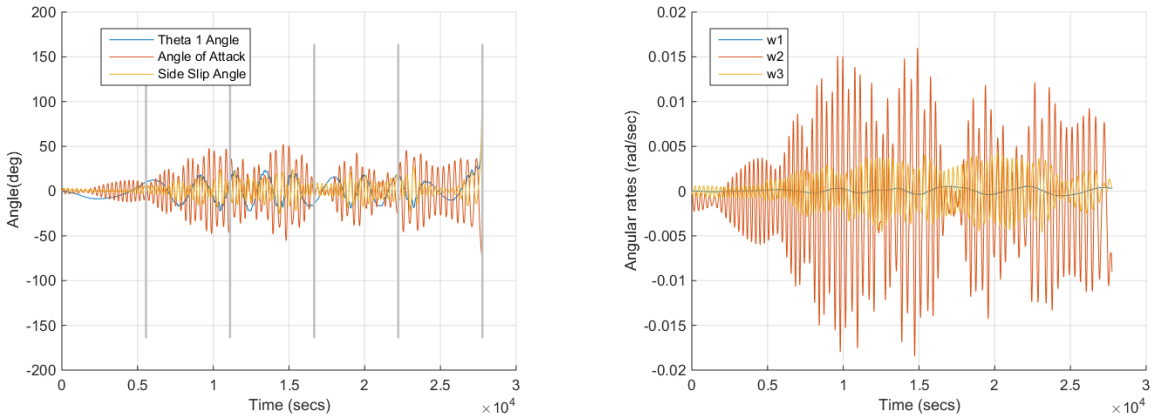

(a) Angle history over 5 orbits

(b) Body fixed angular velocities over 5 orbits

Figure 16: The simulation results for a stable configuration with a clear CP1 sail material. $\phi = 70°$, $h = 400$ km, $\Omega = 10°$.

III.E. Baseline Design

The baseline design will use clear CP1 as the sail membrane to ensure the minimum amount of disturbance from SRP. In terms of shape and size of the device, the goal is to maximize both stability and drag. Table 5 shows that apex half-angle of 85° is stable for all the right ascensions investigated for altitudes below 450 km, and some right ascensions at 500 and 525 km. The deorbit analysis showed that a 125 m^2 drag area will deorbit a 100 kg satellite from 1,200 km and a 150 km satellite from 1,100 km within 25 years, and a 195 m^2 drag area will deorbit a 150 kg satellite from 1,200 km with 25 years. The first case will require the booms to be 8 m long to get a base area of 127 m^2, and the latter case requires the booms to be 10 m long to get a base area of 198 m^2.

IV. Conclusion

Orbital debris is an important issue that should be part of satellite design. This paper proposes a passive aerodynamically stable drag device to be attached to small satellites before launch to ensure that the satellite will deorbit within 25 years without requiring the satellite to survive through deorbit. The stability of the pyramid shaped drag sail is investigated over a five orbit time span at different altitudes subject to disturbance torques created by the gravity gradient, aerodynamics, and solar radiation pressure. It was shown that if one uses normal solar sail membrane materials that are reflective because of an aluminum coating, there are only a few orbits where the sail will be stable. The authors then go on to describe using uncoated materials for the sail, which are clear. This greatly increases the range of orbits where the sail is stable. Finally, the baseline design of the sail was set at an apex half-angle of 85°, with 8 m long booms to ensure that a 100 kg satellite will deorbit from a circular orbit at an altitude of 1,200 km within 25 years. A larger sail is also sized for 150 kg satellites from the same altitude.

Acknowledgments

This work was supported by a NASA Space Technology Research Fellowship. The authors would like to thank Mark Schoenenberger of NASA Langley Research Center, Andrew Heaton of NASA Marshall Space Flight Center and Kenneth Hart of Georgia Institute of Technology for their advice towards the completion of this work. In addition, the authors would like to thank McKenzie Long of Cardinal Innovative for creating the square pyramid graphic.

References

[1] "OneWeb Satellites Company Given Birth By Airbus Defence and Space + OneWeb," [Online] `http://www.satnews.com/story.php?number=214814180`, 2016, Accessed: 2016-07-26.

[2] de Selding, P. B., "SpaceX To Build 4,000 Broadband Satellites in Seattle," [Online] `http://spacenews.com/spacex-opening-seattle-plant-to-build-4000-broadband-satellites/`, Jan 15 2015, Accessed: 2016-07-26.

[3] Masunaga, S., "Boeing applies for license to launch proposed satellite constellation," [Online] `http://www.latimes.com/business/la-fi-boeing-satellites-20160623-snap-story.html`, Jun 23 2016, Accessed: 2016-07-26.

[4] de Selding, P. B., "OneWeb Pledges Vigilance on Orbital Debris Issue," [Online] `http://spacenews.com/oneweb-pledges-vigilance-on-orbital-debris-issue/`, Oct 15 2015, Accessed: 2016-08-01.

[5] Alhorn, D., Casas, J. P., Agasid, E. F., Adams, C., Laue, G., Kitts, C., and O'Brien, S., "NanoSail-D: The Small Satellite that Could!" *25th Annual AIAA/USU Conference on Small Satellites*, Aug. 2011.

[6] Johnson, L., Whorton, M., Heaton, A., Pinson, R., Laue, G., and Adams, C., "NanoSail-D: A solar sail demonstration mission," *Acta Astronautica*, Vol. 68, March 2010, pp. 571–575.

[7] Biddy, C. and Svitek, T., "LightSail-1 Solar Sail Design and Qualification," *Proceedinfs of the 41st Aerospace MEchanisms Symposium*, May 2012.

[8] Davis, J., "LightSail Test Mission Declared Success: First Image Complete," [Online] `http://www.planetary.org/blogs/jason-davis/2015/20150609-lightsail-test-mission-success.html`, Jun 9 2015, Accessed: 2015-09-14.

[9] Long, A. and Spencer, D. A., "Deployable Drag Device for Launch Vehicle Upper Stage Deorbit," *65th International Astronautical Congress*, No. IAC - 14,A6.P,82x25843, Sept. 2014.

[10] Etkin, B., *Dynamics of Atmospheric Flight*, Dover Publications, 2000.

[11] Chavali, D. and Hughes, S., "GMAT Wiki Home," [Online] `http://gmatcentral.org/`, Mar 29 2016, Accessed: 2016-08-02.

[12] Hart, K. A., Dutta, S., Simonis, K. R., Steinfeldt, B. A., and Braun, R. D., "Analytically-derived Aerodynamic Force and Moment Coefficients of Resident Space Objects in Free-Molecular Flow," *AIAA Atmospheric Fligt Mechanics Conference*, No. AIAA 2014-0728, Jan. 2014.

[13] Weisstein, E. W., "Erf." [Online] `http://mathworld.wolfram.com/Erf.html`, Accessed: 2016-08-14.

[14] Wie, B., *Space Vehicle Dynamics and Control*, AIAA Education Series, 2008.

[15] McInnes, C. R., *Solar Sailing: Technology, Dynamics and Mission Applications*, Praxis Publishing, 1999.

[16] John E. Canady, J. and John L. Allen, J., "Illumination From Space with ORbiting Solar-Reflector Spacecraft," Tech. rep., NASA Technical Paper 2065, 1982.